MID-AMERICA TRANSPORTATION CENTER

Report # MATC-MS&T: 139-4

Final Report

WBS: 25-1121-0005-139-4

A Dynamic Hurricane Risk Modeling Framework to Improve Bridge Safety Under Changing Climate

Grace Yan, PhD
Associate Professor
Department of Civil, Architectural and Environmental Engineering
Missouri University of Science and Technology

2024

A Cooperative Research Project sponsored by U.S. Department of Transportation- Office of the Assistant Secretary for Research and Technology

MATC

A Dynamic Hurricane Risk Modeling Framework to Improve Bridge Safety Under Changing Climate

Grace Yan, PhD
Professor
Department of Civil, Architectural and Environmental Engineering
Missouri University of Science and Technology

A Report on Research Sponsored by

Mid-America Transportation Center
University of Nebraska–Lincoln

September 2024

Technical Report Documentation Page

1. Report No. 25-1121-0005-139-4	2. Government Accession No.	3. Recipient's Catalog No.
4. Title and Subtitle A Dynamic Hurricane Risk Modeling Framework to Improve Bridge Safety Under Changing Climate		5. Report Date September 2024 6. Performing Organization Code
7. Author(s) Grace Yan		8. Performing Organization Report No.
9. Performing Organization Name and Address Missouri University of Science and Technology 1401 N. Pine St. Rolla, MO 65401		10. Work Unit No. (TRAIS) 11. Contract or Grant No. 69A3551747107
12. Sponsoring Agency Name and Address Office of the Assistant Secretary for Research and Technology 1200 New Jersey Ave., SE Washington, D.C. 20590		13. Type of Report and Period Covered Final Report January 2022 – June 2024 14. Sponsoring Agency Code MATC TRB RiP No. 91994-109
15. Supplementary Notes		

16. Abstract

Coastal regions have been experiencing more frequent and more intensive tropical cyclones (TCs) due to climate change in recent years. In 2020, the tropical storms in the Atlantic Ocean made a number record in a season, with 30 named storms in total, 13 of which progressed into hurricanes. Global warming will continue and climate change will follow (USGCRP, 2018), leading to more severe winds and storms and threating the safety of bridges in coastal regions. In order for local governments to take pro-active adaptations and measures, it is essential to understand the local impact of global climate change. To address this, this project will develop a new, efficient hurricane wind model, which can help determine the wind speed in the local region, before and after TCs make landfall. This will inform decision-makers when they develop near-term measures and long-term plans for mitigation and adaptation to climate change. To achieve this research goal, by balancing the advantages and disadvantages of existing parametric TC models for engineering applications, this project will develop a high-fidelity, computationally efficient three-dimensional nonlinear TC model that can consider the varying land cover and terrains without too much simplification of the kinetic equations. The obtained results can be used to improve the AASHTO Bridge Design Specifications periodically to accommodate the future climate change, enhancing the resilience of bridges.

17. ORCID No. of each Researcher		18. Distribution Statement	
19. Security Classif. (of this report) Unclassified	20. Security Classif. (of this page) Unclassified	21. No. of Pages 36	22. Price

Table of Contents

List of Figures

List of Tables

Disclaimer

The contents of this report reflect the views of the authors, who are responsible for the facts and the accuracy of the information presented herein. This document is disseminated in the interest of information exchange. The report is funded, partially or entirely, by a grant from the U.S. Department of Transportation's University Transportation Centers Program. However, the U.S. Government assumes no liability for the contents or use thereof.

Acknowledgments

Numerical simulations in this project were performed using the Foundry cluster at the Missouri University of Science and Technology, which is supported by the National Science Foundation under Grant No. OAC-1919789. The authors appreciate the financial support from the Mid-American Transportation Center, through the MATC project, titled “A Dynamic Hurricane Risk Modeling Framework to Improve Bridge Safety under Changing Climate”.

Abstract

Coastal regions have been experiencing more frequent and more intensive tropical cyclones (TCs) due to climate change in recent years. In 2020, the Atlantic Ocean made a new seasonal record of tropical storms, with 30 named storms in total, 13 of which progressed into hurricanes. Global warming will continue, and climate change will follow (USGCRP, 2018), leading to more severe winds and storms and threating the safety of bridges in coastal regions. In order for local governments to take pro-active adaptations and measures, it is essential to understand the local impact of global climate change. To address this, this project will develop a new, efficient hurricane wind model, which can help determine the wind speed in the local region, before and after TCs make landfall. This will inform decision-makers when they develop near-term measures and long-term plans for mitigation and adaptation to climate change. To achieve this research goal, by balancing the advantages and disadvantages of existing parametric TC models for engineering applications, this project will develop a high-fidelity, computationally efficient three-dimensional nonlinear TC model that can consider the varying land cover and terrains without too much simplification of the kinetic equations. The obtained results can be used to improve the AASHTO Bridge Design Specifications periodically to accommodate future climate change, enhancing the resilience of bridges.

Chapter 1 Research Motivation and Significance

Parametric tropical cyclone (TC) models have been widely used in simulating TC wind fields for engineering applications and insurance appraisals. Previously, these parametric models estimated the TC wind speed near the surface by first multiplying the wind speed at gradient height by a reduction factor and then projecting the reduced wind speed to reflect the near-surface condition. For example, Batts et al. (1980) took 0.865 as the reduction factor, which was the ratio of ocean surface wind speed (at the height of 10 m) to the gradient wind speed, while Georgiou et al. (1983) found that this ratio should vary with the radial distance from TC center, with 0.85 used near the TC eyewall and 0.65 used away from the TC eyewall. Later on, mean boundary layer wind speed models (known as slab models) were developed (Thompson and Cardone, 1996; Vickery et al., 2000). However, this kind of model lacked essential physical processes in the boundary layer, e.g. the vertical advection and diffusion processes.

To overcome the disadvantages of the slab models, the height resolving TC models were developed to include the vertical diffusion and/or advection processes through either a linear method (Kepert, 2001; Meng et al, 1995) or a nonlinear method (Kepert and Wang, 2001). The nonlinear method described in Kepert and Wang (2001) was to develop a three-dimensional TC model with a higher-order boundary layer turbulence closure scheme, which was known as the Mellor-Yamada level $2^1/_4$ scheme. This nonlinear TC model can well capture the spatial structure of wind speed of TCs, including the super-gradient wind speed and the logarithmic near-surface wind speed profile. However, it is very time-consuming. On the contrary, the linearized height resolving models (Kepert, 2001; Meng et al, 1995) that considered the essential vertical diffusion process were computationally efficient. These linearized models can directly describe the wind speed distribution along the height (referred to as “vertical wind profile” in the following).

However, due to the negligence of vertical advection, the jet height (height of maximum wind speed) and jet strength (maximum wind speed) estimated from the linearized models are lower and smaller than those of the nonlinear models (Kepert and Wang, 2001) and observations (Franklin et al., 2003). In addition, when a constant vertical eddy viscosity coefficient (K_V) is used, these linearized models may lead to a linear, rather than logarithmic, vertical wind profile in the near-surface layer (Kepert, 2012). Furthermore, calibration of the vertical eddy viscosity coefficient using the observed data (Fang et al., 2018a) is also limited compared to the use of a nonlinear method with a suitable turbulence closure model (Hong et al., 2019; Meng et al., 1997).

Despite the previous research, most of the parametric TC models are built on flat land or sea surfaces (Hong et al., 2019; Vickery et al., 2009; Wu and Huang, 2019), which are not consistent with real-world situations. To improve TC modeling, the influence of inhomogeneous terrains on TC wind fields should not be ignored, especially for mountainous countries. In the HAZUS-MH hurricane model, Vickery et al. (2006) developed a terrain model that considered land use and land cover, but did not include the effect of regional topography. More recently, Done et al. (2020) generated a dataset of 714 global historical TC footprints by using a modified TC model of Kepert and Wang (2001), and the effects of terrain features and varying land surface friction were directly included in the kinetic equations, rather than using simple factors based on the terrain types and wind directions (Tan and Fang, 2018).

The objective of this research is to develop a high-fidelity, high-efficiency three-dimensional nonlinear TC model that can consider the varying land cover types and terrains without too much simplification of the kinetic equations. This projects aims to do this by balancing the advantages and disadvantages of existing parametric TC models. To be specific,

this model is developed based on the kinetic equations similar to Kepert and Wang (2001), while a nested grid system with higher computational efficiency is applied. A terrain-following coordinate system proposed by Gal-Chen and Somerville (1975) is adopted here to consider terrain changes, and the surface layer parameterization scheme proposed by Meng et al. (1995) is adopted to consider the varying land cover types. Additionally, the Louis boundary layer scheme is chosen to calculate the vertical eddy viscosity coefficient based on the Kepert (2012)'s comparison results of four different boundary layer parameterization schemes. In this report, detailed descriptions of the simulation method and model setup will be provided in Chapter 2, including the sensitivity studies on different simulation durations and horizontal grid systems. In Chapter 3, model validations against the H*Wind snapshots and surface station observations will be provided in Chapter 3. Finally, in Chapter 4, conclusions will be drawn, and future work will be suggested.

Chapter 2 Modeling Method and Simulation Setup

2.1 Governing equations

Although the thermal effect is a contributing factor in TC evolutions, it can be ignored when investigating the dynamic behavior of a mature TC especially in the atmospheric boundary layer. The governing equations of this numerical TC model are simplified by the Boussinesq approximation and Reynolds Averaging, which can be written in the Cartesian coordinate system with the origin at TC center (shown in Figure 2.1), as described by Holton (2007)

$$\frac{du}{dt} = -\frac{1}{\rho_0}\frac{\partial p}{\partial x} + f \cdot v - \left(\frac{\partial u'u'}{\partial x} + \frac{\partial u'v'}{\partial y} + \frac{\partial u'w'}{\partial z} \right) \tag{1}$$

$$\frac{dv}{dt} = -\frac{1}{\rho_0}\frac{\partial p}{\partial y} - f \cdot u - \left(\frac{\partial v'u'}{\partial x} + \frac{\partial v'v'}{\partial y} + \frac{\partial v'w'}{\partial z} \right) \tag{2}$$

$$\frac{\partial u}{\partial x} + \frac{\partial v}{\partial y} + \frac{\partial w}{\partial z} = 0 \tag{3}$$

$$p = p_c + \Delta p \cdot \exp\left[-\left(\frac{R_{max}}{r} \right)^B \right] \tag{4}$$

where d/dt denotes the rate of velocity change, which is expressed as, $\frac{d}{dt} = \frac{\partial}{\partial t} + u_c\frac{\partial}{\partial x} + v_c\frac{\partial}{\partial y} + u\frac{\partial}{\partial x} + v\frac{\partial}{\partial y} + w\frac{\partial}{\partial z}$; u, v and w (m/s) are wind velocity components in the x, y and z (m) directions, respectively; u', v' and w' (m/s) are the fluctuating components of u, v and w, respectively; u_c and v_c (m/s) are TC moving velocity components in the x and y directions; ρ_0 (kg/m^3) is the density of air; f (s^{-1}) is the Coriolis parameter; r (m) is the radial distance from the TC center; p (Pa) is the atmospheric pressure at r; p_c (Pa) is the pressure at the TC center; Δp (Pa) is the difference between the pressure at the TC center and standard atmospheric pressure (1010

hPa used in this project); R_{max} (m) is the radius where the maximum wind speed is observed; and B is the Holland's pressure profile parameter. In this project, R_{max} and B are obtained based on Vickery and Wadhera (2008) and expressed as

$$R_{max} = exp(3.015 - 6.291\times10^{-5}\Delta p^2 + 0.0337\cdot lat) \tag{5}$$

$$B = 1.833 - 0.326\sqrt{f\cdot R_{max}} \tag{6}$$

where *lat* is the latitude of TC center. Although previous studies (Fang et al., 2018b; Snaiki and Wu, 2017b) have discussed the variations of the pressure field with height, in this project, it is assumed that the air density is constant and the thermal effect is negligible. Thus, in this TC model, the pressure field does not change with height, and the analytical pressure profile of Holland (1980) (Eq. (4)) is applied to the entire model computational domain.

It should be noted that the governing equations (Eq. (1) – Eq. (3)) are based on a computational domain with flat ground surface, and they will be transformed to solve in a terrain-varying situation using the terrain-following coordinate system described in Section 2.3.

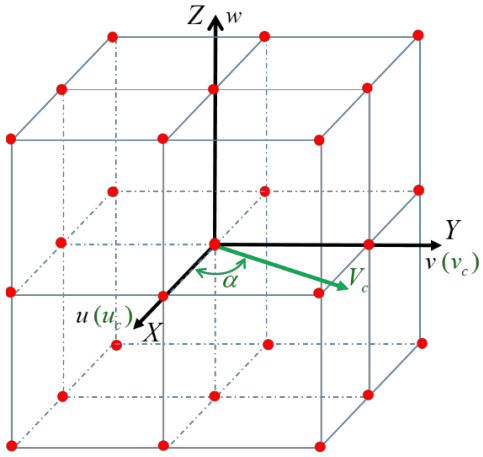

Figure 2.1 Cartesian coordinate system (V_c is the resultant TC moving velocity; α denotes the TC moving direction).

Based on the turbulence closure scheme, referred to as *K theory*, the horizontal and vertical turbulent flux terms in Eq. (1) and Eq. (2) are expressed as (Holton, 2007)

$$-\left(\frac{\partial u'u'}{\partial x}+\frac{\partial u'v'}{\partial y}+\frac{\partial u'w'}{\partial z}\right)=\frac{\partial}{\partial x}\left(K_H\frac{\partial u}{\partial x}\right)+\frac{\partial}{\partial y}\left(K_H\frac{\partial u}{\partial y}\right)+\frac{\partial}{\partial z}\left(K_V\frac{\partial u}{\partial z}\right) \tag{7}$$

$$-\left(\frac{\partial v'u'}{\partial x}+\frac{\partial v'v'}{\partial y}+\frac{\partial v'w'}{\partial z}\right)=\frac{\partial}{\partial x}\left(K_H\frac{\partial v}{\partial x}\right)+\frac{\partial}{\partial y}\left(K_H\frac{\partial v}{\partial y}\right)+\frac{\partial}{\partial z}\left(K_V\frac{\partial v}{\partial z}\right) \tag{8}$$

where K_H and K_V (m^2/s) are the horizontal and vertical eddy viscosity coefficients, respectively. According to Smagorinsky et al. (1965) and Grell et al. (1994), K_H is given by

$$K_H=2\kappa^2\left(\frac{\Delta x}{2}\right)^2\cdot\left[\left(\frac{\partial u}{\partial x}-\frac{\partial v}{\partial y}\right)^2+\left(\frac{\partial v}{\partial x}+\frac{\partial u}{\partial y}\right)^2\right]^{1/2} \tag{9}$$

where Δx (m) is the grid point spacing; κ is the von Kärmän's constant, and κ=0.4 is adopted here. The vertical eddy viscosity coefficient K_V is also important, because it controls the vertical wind profile of a TC. Based on the comparison results of Kepert (2012), the modified Louis boundary layer scheme is used

$$K_V=l^2\left[\left(\frac{\partial u}{\partial z}\right)^2+\left(\frac{\partial v}{\partial z}\right)^2+10^{-9}\right]^{1/2} \tag{10}$$

where $l=1\Big/\left[(\kappa z)^{-1}+l_\infty^{-1}\right]$, l_∞ is the asymptotic mixing length, and l_∞=80m. In this TC model, the initial value of K_V is set as $10m^2/s$.

2.2 Boundary conditions

On the top boundary in Figure 2.2, u, v and w are assumed not to change with height, and accordingly

$$\frac{\partial u}{\partial z} = \frac{\partial v}{\partial z} = \frac{\partial w}{\partial z} = 0 . \tag{11}$$

On the bottom boundary in Figure 2.2, the balance between the dissipation and production of surface momentum flux is adopted

$$K_V \left(\frac{\partial u}{\partial z} \right)_{z \to 0} = C_D \cdot \sqrt{\left(u + u_c\right)^2 + \left(v + v_c\right)^2} \cdot \left(u + u_c\right) \tag{12}$$

$$K_V \left(\frac{\partial v}{\partial z} \right)_{z \to 0} = C_D \cdot \sqrt{\left(u + u_c\right)^2 + \left(v + v_c\right)^2} \cdot \left(v + v_c\right) \tag{13}$$

$$C_D = \frac{\kappa^2}{\left\{ \ln\left[\left(z_1 + 2.85 z_0^{0.86} \right) / z_0 \right] \right\}^2} \tag{14}$$

where C_D is the drag coefficient that is calculated using the surface layer parameterization scheme given in Meng et al. (1995); z_0 is the surface roughness length, which can be determined by the type of local land cover; z_1 is the height of the lowest model layer, and z_1=1m is adopted.

After testing several lateral boundary condition schemes (e.g. the radiation boundary conditions that were proposed by Orlanski (1976) and used in Kepert and Wang (2001), and the Ekman boundary conditions that were used in Hong et al. (2019)), the present authors find that the simulation results are affected little by the lateral boundary conditions in this TC model. In this project, modified Ekman lateral boundary conditions are chosen, and the wind flow

acceleration terms, horizontal advection terms and horizontal diffusion terms are assumed to be negligible.

$$\left(\frac{\partial}{\partial t}+u_c\frac{\partial}{\partial x}+v_c\frac{\partial}{\partial y}+u\frac{\partial}{\partial x}+v\frac{\partial}{\partial y}+w\frac{\partial}{\partial z}\right)\cdot(u,v)=0 \tag{15}$$

$$\frac{\partial}{\partial x}\left(K_H\frac{\partial}{\partial x}\right)\cdot(u,v)+\frac{\partial}{\partial y}\left(K_H\frac{\partial}{\partial y}\right)\cdot(u,v)=0 \tag{16}$$

Then, Eq. (1) and Eq. (2) can be rewritten as

$$-\frac{1}{\rho_0}\frac{\partial p}{\partial x}+f\cdot v+\frac{\partial}{\partial z}(K_V\frac{\partial u}{\partial z})=0 \tag{17}$$

$$-\frac{1}{\rho_0}\frac{\partial p}{\partial y}-f\cdot u+\frac{\partial}{\partial z}(K_V\frac{\partial v}{\partial z})=0 \tag{18}$$

where K_V=10m^2/s.

In addition, the vertical wind component w is taken as 0m/s at the bottom and outermost boundaries.

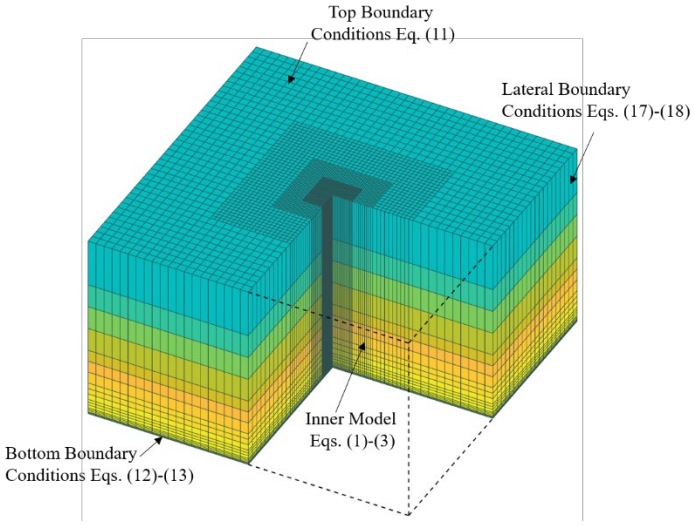

Figure 2.2 Computational domain of the developed TC model and boundary conditions.

2.3 Grid system and coordinate transformation

The governing equations (Eqs. (1)-(3)) can discretized and numerically integrated over a three-dimensional grid system. Considering that the wind speed changes rapidly around R_{max} and the turbulent flux decreases with height, to improve the computational efficiency, the grid system (Figure 2.3) is set to provide a relatively high resolution (small grid spacing) near the inner region of a TC and near the ground surface, and low resolution (large grid spacing) in the outer region and the upper region of the computational domain.

A four-level nested grid system is used in the computational domain, as shown in Figure 2.3(a). The mesh size remains constant within each nest. The grid point spacing of the outer nest is twice that of the adjacent inner one. Each nest has 20 grid points from the TC center. For example, if the grid point spacing in the innermost nest is set to be dx=dy=0.1R_{max}, the grid point spacing in the second to fourth nests are 0.2R_{max}, 0.4R_{max} and 0.8R_{max}, respectively. The entire computational domain can cover an area of 32R_{max}×32R_{max} on the horizontal plane, which is large enough to capture the wind characteristics of TCs.

In the vertical direction, the computational domain is divided into 20 layers, including 7 layers from 0 to 100 m (1, 10, 20, 30, 50, 70, 90 m), 9 layers from 100 to 1000 m (130, 170, 210, 290, 370, 450, 610, 770, 930 m), and 4 layers above 1000 m (1250, 1570, 1890, 2530 m), as shown in Figure 2.3(b). The vertical grid system below 100m has a higher resolution, which is designed to meet the need of engineering applications, because most buildings are lower than 100 m.

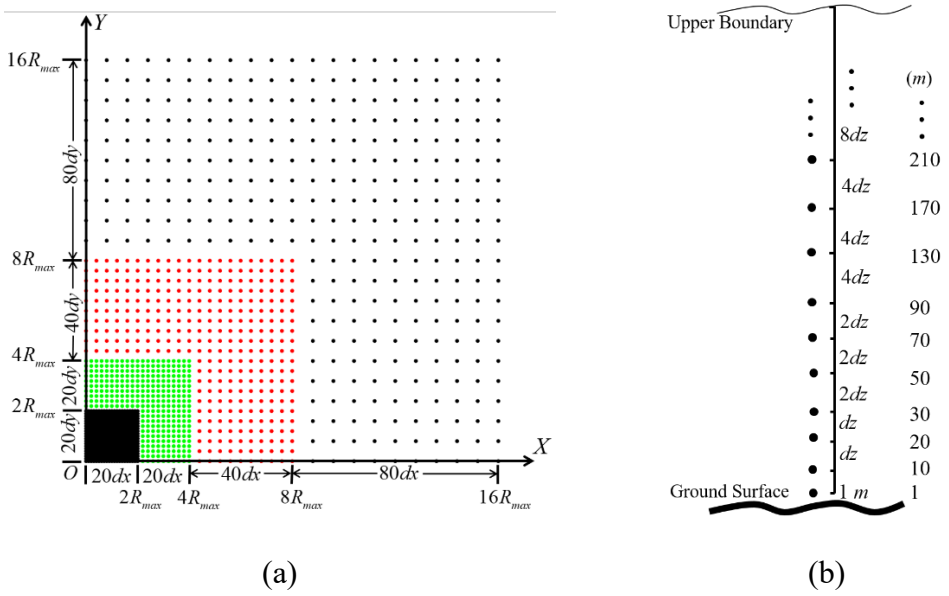

(a) (b)

Figure 2.3 Schematic diagram of the nested grid system. (a) Horizontal nested grid system for the first quadrant with dx=dy=0.1R_{max} as an example. (b) Vertical grid system with dz=10m.

A coordinate transformation method proposed by Gal-Chen and Somerville (1975) is used in this project to transform the governing equations (Eqs. (1)-(3)) into a terrain-following coordinate system, referred to as sigma coordinate. This terrain-following coordinate system (u_T, v_T, w_T) can be expressed in terms of (x, y, z) as

$$x_T = x\,,\ y_T = y\,,\ z_T = H \cdot \frac{z - z_s(x,y)}{H - z_s(x,y)}\,, \tag{19}$$

where $z_s(x, y)$ is the terrain height at (x, y); H is the vertical extent height, and it means that above this height the terrain effects are ignored. H=20km is adopted, where the atmospheric pressure is 50hPa, which is the top of the WRF model (Skamarock et al., 2019). The wind components u, v and w are also transformed to u_T, v_T and w_T in this terrain-following coordinate system by

$$u = u_T\,,\ v = v_T\,,\ w = \frac{\partial z_s}{\partial x}\frac{H - z_T}{H}u_T + \frac{\partial z_s}{\partial y}\frac{H - z_T}{H}v_T + \frac{H - z_s}{H}w_T\,. \tag{20}$$

2.4 Solution procedure

For a computational domain shown in Figure 2.2, the wind velocity components, u, v and w, are defined at each grid point, and the horizontal and vertical eddy viscosity coefficients (K_H and K_V) are defined at cell centers. In Equations (1)-(3), the first-order upwind difference scheme is adopted to approximate the advection terms and the second-order central difference scheme is used for the diffusion terms. For integration, an explicit forward time scheme is used, and the Coriolis force terms are treated implicitly to dampen inertial oscillations. More specifically, Equation (1) and Equation (2) can be discretized as

$$\frac{u^{\tau+1} - u^{\tau}}{\Delta t} + advection\ terms = -\frac{1}{\rho_0}\frac{\partial p}{\partial x} + f \cdot v^{\tau+1} - diffusion\ \ terms \tag{21}$$

$$\frac{v^{\tau+1}-v^{\tau}}{\Delta t}+advection\ terms=-\frac{1}{\rho_0}\frac{\partial p}{\partial y}-f\cdot u^{\tau+1}-diffusion\ \ terms \tag{22}$$

where Δt is the time increment; and τ is the computation index, which starts from 0.

To facilitate computation convergence, the computational time increment for the innermost nested grid is set as Δt=1s, and Δt for the second, third and fourth nest grids are 2s, 4s and 8s, respectively. $\Delta t/dx$ remains constant at each nested grid (Chow, 1971). Therefore, for a simulation duration of t=8s (t=Δt×iteration times), the fourth nested grid only needs to iterate once, the third nested grid needs to iterate twice, and the second and first nested grids need to iterate four times and eight times, respectively. In addition, the lateral boundary conditions for the inner nested grid are determined by the adjacent outer nested grid at every computational step, and a diagonal upwind differencing is adopted to reduce the computational errors of the advection terms (Chow, 1971).

The computation of this TC model starts from the lowest model layer and proceeds upward; for horizontal grids, the computation starts from the outermost nested grid and proceeds into the innermost grid. Winds in gradient balance is applied as the initial condition. The gradient wind v_g calculated from the gradient balance with the prescribed pressure field (Eq. (4)) is given by Vickery and Wadhera (2008).

$$v_g=\left\{\left(\frac{R_{max}}{r}\right)^{B}\frac{B\Delta p}{\rho_0}\exp\left[-\left(\frac{R_{max}}{r}\right)^{B}\right]+\left(\frac{rf}{2}\right)^{2}\right\}^{1/2}-\frac{rf}{2}. \tag{23}$$

Time scale of the steady-state simulated wind speed is consistent with the Reynolds averaging time interval of the governing equations (Eqs. (1)-(3)), which should be long enough to filter out small-scale eddy fluctuations within the boundary layer (Holton, 2007). Thus, the

averaging period of wind speeds is set as one hour in this study, and the input parameters are also interpolated linearly into a one hour scale.

2.5 Land cover and terrain data

As shown in Equation (14), this TC model can be applied to different land cover through changing the surface roughness length. The surface roughness length can be obtained based on the global land cover datasets. To date, nine global land cover datasets have been generated by different initiatives using satellite data (Yang et al., 2017). Although these land cover datasets can reflect different types of Earth's surface, there are some differences due to different satellite data and classification schemes. Yang et al. (2017) studied the similarities and discrepancies of seven out of nine global land cover datasets by comparing the area and spatial patterns of different land cover datasets over China. They found that the CCI-LC 2010/2000 produced by the European Space Agency (ESA) Climate Change Initiative (CCI) has a very high accuracy. Therefore, the latest land cover version of CCI-LC 2018 (ESA, 2017) is adopted in this study.

The land cover types used in this study is from the CCI-LC 2018, as listed in Table 2.1, where the corresponding roughness length for each type of land cover was extracted from the WRF (listed in LANDUSE.TBL). The roughness length over the Pearl River Delta is plotted based on the data provided in CCI-LC 2018, as shown in Figure 2.4(a). Considering that the Gridded Bathymetry Data produced by the Generalized Bathymetric Chart of the Oceans (GEBCO) provides the latest high resolution terrain height, the GEBCO_2020 that provides the information of z_s is used in Equations (19) and (20). The map of terrain over the Pearl River Delta is shown in Figure 2.4(b).

Table 2.1 Land cover lookup table of CCI-LC 2018

Land Cover Types	Roughness Length (m)
Rainfed Cropland	0.15
Irrigated Cropland	0.10
Cropland (>50%)/Natural Vegetation (<50%)	0.14
Cropland (<50%)/Natural Vegetation (>50%)	0.14
Tree Cover (Evergreen)	0.50
Tree Cover (Deciduous)	0.50
Tree Cover (Needle leaved, Evergreen)	0.50
Tree and Shrub (>50%)/Herbaceous Cover (<50%)	0.50
Tree and Shrub (<50%)/Herbaceous Cover (>50%)	0.50
Shrub Land	0.05
Grass Land	0.12
Sparse Vegetation	0.01
Tree Cover (Fresh/Brackish Water)	0.40
Tree Cover (Saline Water)	0.40
Shrub / Herbaceous Cover (Flooded)	0.20
Urban Areas	0.80
Water Bodies	0.0002

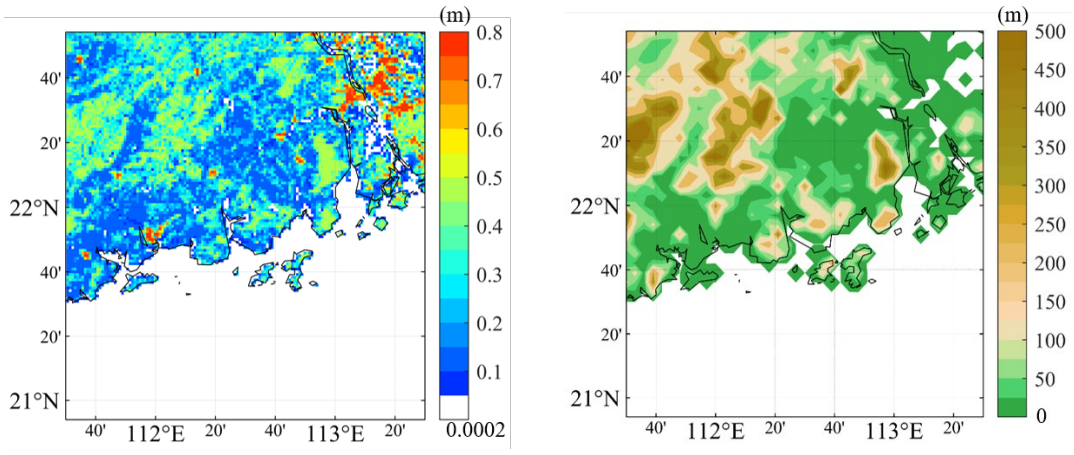

(a) (b)

Figure 2.4 (a) Roughness length of different land cover types; (b) Terrain over the Pearl River Delta.

2.6 Sensitivity analysis

2.6.1 Determination of the simulation duration

The developed TC model is initialized with the gradient wind (v_g from Eq. (23)) and the pressure field (Eq. (4)), then the wind flow in the computational domain is simulated through iterations. According to Kepert and Wang (2001), the simulation duration of 24 hours is needed for the simulation to reach a steady state, while Done et al. (2020) found the near-ground wind attains a steady state much faster. To determine the simulation duration in this study, four TC simulation cases listed in Table 2.2 are carried out.

In this project, 48 hours of simulation duration are used in all four simulated cases to ensure that it is long enough for the simulated TC wind flow to reach a steady state. The simulated wind speeds obtained from 0 to 24 hours are compared with the result at the 48th hour to find out the minimum simulation duration that can produce satisfactory results. To be specific, the root mean square errors (RMSE) of the simulated wind speed at each hour are compared with the wind speed obtained at the 48th hour and presented in Figure 2.5 as blue graphs.

The RMSE rapidly decreases in the first hour and reaches about 25% of its initial value (the RMSE value at 0 hour), as indicated by the orange graphs in Figure 2.5. Then it takes nearly nine hours to reach 10% of the corresponding RMSE initial value. The minimum RMSE occurs at about the 16th hour, then it increases slightly. Considering that the RMSE value at the 24th hour is only slightly smaller than that at the 10th hour and it is very time consuming to run for 24 hours, the simulation duration of 10 hours is adopted. It takes nearly 20 minutes to complete the 10 hours' simulation of one case using a single core on the i7 PC platform. The results presented in this report are based on the simulation duration of 10 hours.

Table 2.2 Parameters of TC simulation cases

TC (Case)	p_c (hPa)	R_{max} (km)	B	lat (°)	V_c (m/s)	α (°)	z_0 (m)	Max gradient wind (m/s)
I	969.61	40	1.3	20	0	90	0.0002	40
II	969.61	40	1.3	20	5	90	0.0002	40
III	959.21	40	1.6	20	5	90	0.0002	50
IV	920.56	40	1.3	20	5	90	0.0002	60

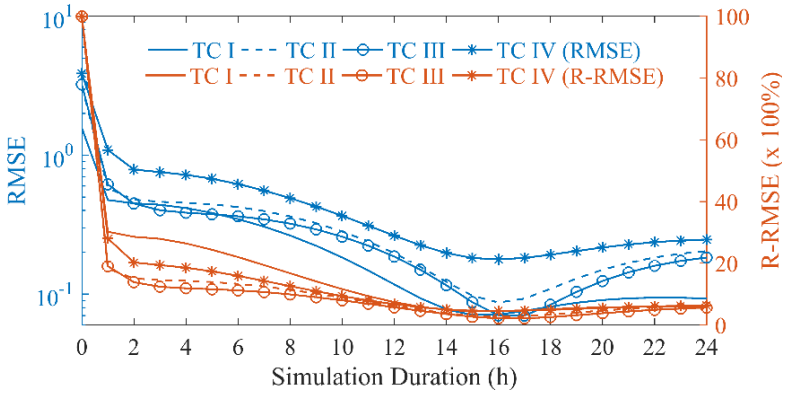

Figure 2.5 Errors of the simulated wind speeds at each hour compared with the steady state (simulation results at the 48th hour). The left y-axis is the root mean square error (RMSE), and the right y-axis is the relative RMSE (R-RMSE), which is the ratio of RMSE/(RMSE at 0 hour).

2.6.2 Determination of the horizontal grid system

To investigate the influence of the grid size on simulation results, besides the grid system presented in Figure 2.3, three additional horizontal grid systems are considered, as shown in Figure 2.6. Case I (TC I listed in Table 2.2) is simulated with the four different grid systems, and the obtained azimuthally averaged resultant velocity contours on a vertical plane through the

center of TC in each grid system are presented in Figure 2.6. By comparing Figure 2.6(b) and Figure 2.6(d), with the same minimum grid size (dx=dy=4 km), the nested grid system (Figure 2.6(b)) produces similar results in the inner domain near R_{max} to the uniform grid system (Figure 2.6(d)), and the relative error of the maximum wind speed between the two grid systems is minimal. It is worth noting that the efficiency of the nested grid system is nearly 10 times higher than that of the uniform grid system in this TC simulation.

Among the cases with three different nested grid systems, the azimuthally averaged resultant velocity near R_{max} obtained in the case with dx=dy=2km (Figure 2.6(a)) is much greater than those obtained in the other two cases. However, as the distance from TC center increases, the simulation results become more similar among all three cases. The large wind speed obtained in Figure 2.6(a) may be because a high-resolution grid system tends to generate stronger convection, especially near the TC eyewall, where the magnitude of resultant velocity changes rapidly, associated with a high resultant velocity gradient. In addition, the parameterization schemes of horizontal and vertical turbulent flux used in Eq. (9) and Eq. (10) are mainly applied in the mesoscale atmospheric simulations (Grell et al., 1994; Smagorinsky et al., 1965), which may not suitable for small scale flow. The contours of azimuthally averaged resultant velocity obtained in the case with dx=dy=4km (Figure 2.6(b)) are very similar to those obtained in the case with dx=dy=8km (Figure 2.6(c)). Although the smaller grid size tends to provide more accurate results, it demands more computational resources. To balance the computational accuracy and computational resources, the dx=dy=0.1R_{max}=4km is adopted in the following simulations.

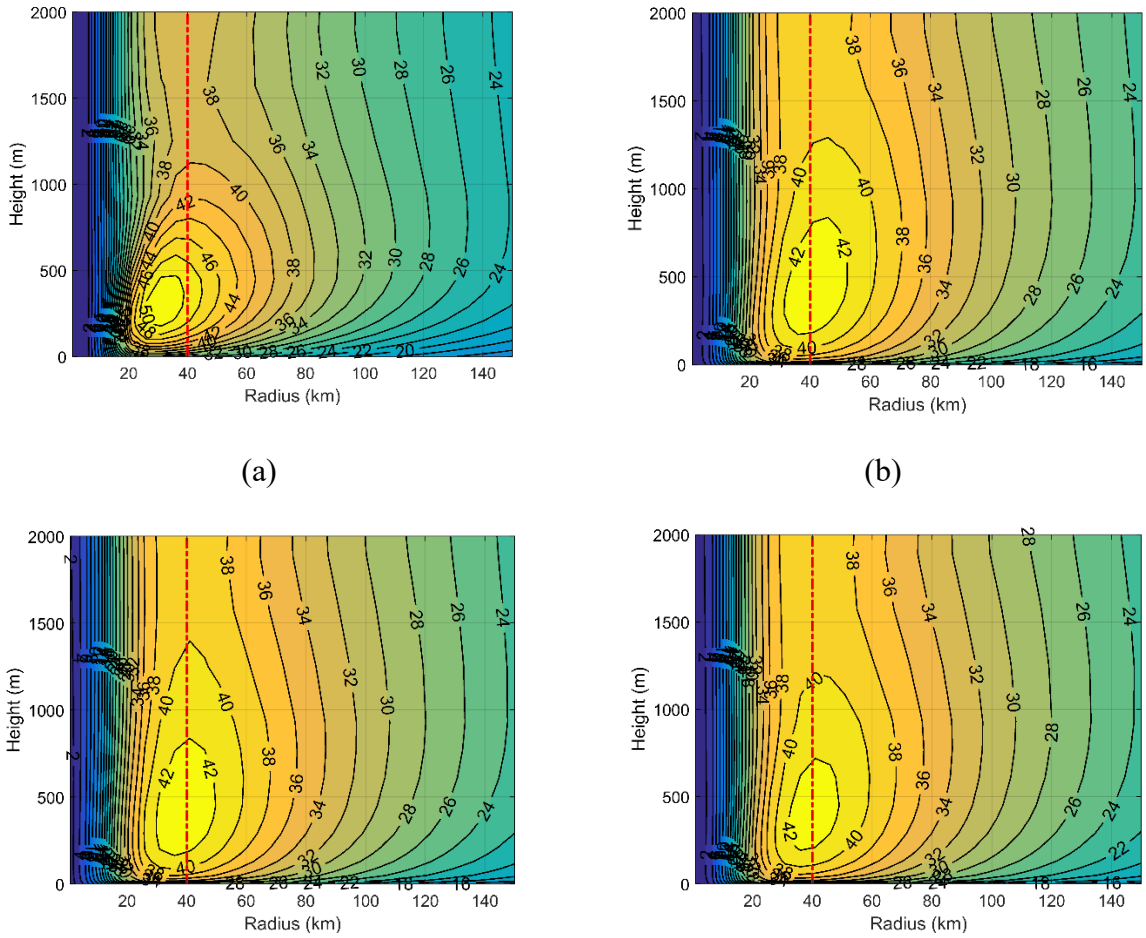

Figure 2.6 Azimuthally averaged resultant velocity contours on a vertical plane in the simulated TC I with four different grid systems. (a) Nested grid system with dx=dy=0.05R_{max}=2km. (b) Nested grid system with dx=dy=0.1R_{max}=4km (The same grid system as in Figure 2.3). (c) Nested grid system with dx=dy=0.2R_{max}=8km. (d) Uniform grid system, grid spacing is 4 km. The red dash line represents R_{max}.

Chapter 3 Simulation Results of TCs under Different Conditions

3.1 Wind speed profile along height (Vertical wind profile)

The GPS dropsonde observations were used to study the wind flow structures of TCs on the vertical plane by many scholars (Franklin et al., 2003; Giammanco et al., 2013; Powell et al., 2003; Vickery et al., 2009). These studies show that the mean vertical wind profile (from a number of TC events) nearly follows the log law below about 300 m. As height increases, the log law breaks down, and the wind speed begins to decrease with the increase of height. Using the vertical wind profiles measured by GPS dropsonde during the 1997-2003 hurricane seasons, Vickery et al. (2009) evaluated the vertical wind profiles of the mean horizontal wind speed near R_{max}. Specifically, the observed vertical wind profiles were divided into different groups based on the R_{max} values and the vertically averaged horizontal wind speed (from heights of 10 m to 500 m). In each group, a mean vertical wind profile was obtained, and through curve-fitting, an empirical logarithmic formula was obtained to model the mean vertical wind profile, which was expressed as

$$U(z) = \frac{u_*}{\kappa}\left[\ln\left(\frac{z}{z_0}\right) - a\left(\frac{z}{H^*}\right)^n\right] \tag{24}$$

where u_* is the friction velocity; H^* is the boundary layer height parameter; a and n are parameters where a=0.4, n=2.0 (Vickery et al., 2009).

In the developed TC model, the vertical wind profile is extracted at R_{max} from TC I simulated with the nested grid size of dx=dy=0.1R_{max}=4 km (Figure 2.6(b)), as indicated by the black graph in Figure 3.1. The vertical wind profile is also obtained by substituting the parameters of TC I listed in Table 2.2 into Equation (24), as indicated by the red dashed graph in

Figure 3.1. These two profiles are similar in terms of the logarithmic feature at lower elevations (below 300 m). The maximum wind speed does not match well, because the empirical equation presents the averaged characteristics of a number of real-world TCs, while the developed TC model is to simulate a scenario of a specific TC, which is expected. Considering that K_V was often set as a constant coefficient in most previous TC models (Kepert, 2001; Meng et al., 1995; Snaiki and Wu, 2017a), one extra case with K_V=10 m^2/s is also simulated. The vertical wind profile with a constant K_V value (10 m^2/s) is extracted and presented in Figure 3.1. It shows that the constant K_V value (blue graph in Figure 3.1) can lead to a nearly linear variation of wind speed with a height near the ground surface, and the maximum wind is much larger than that in the other two cases. This indicates that applications of the constant K_V value may not be proper.

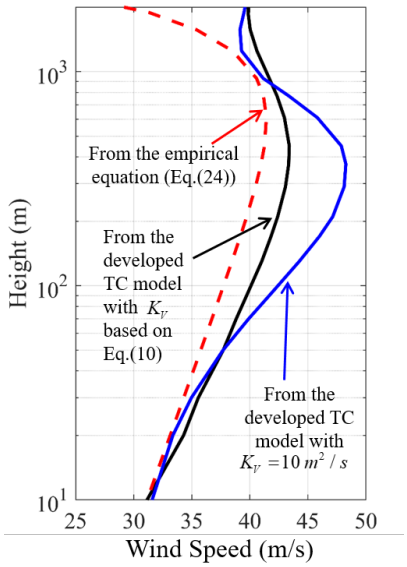

Figure 3.1 Vertical wind profile of TC I at R_{max} (black graph) and its comparisons with the one obtained from the empirical equation (red dashed graph) and the one from the developed TC model with K_V=10m^2/s (blue graph).

3.2 Simulation of TC moving over the ocean

The wind characteristics of TC over the ocean are essential to assess the TC risks to offshore structures, such as offshore oil platforms, offshore wind turbines and sea-crossing bridges. Through assimilating disparate observation data, the H*Wind snapshots were produced by the Hurricane Research Division (Powell et al., 1998), and have been used to evaluate the newly developed or modified TC wind field models (Fang et al., 2018a; Li and Hong, 2015). In this section, the obtained simulation results are compared with the H*Wind snapshots for three TC scenarios (Hurricane Katrina (2005) and Hurricane Irene (2011)) over the ocean at the height of 10 m.

For these two hurricane scenarios, one-minute snapshots sustained resultant velocity distributed on the horizontal plane at the height of 10 m are first obtained. Then, the snapshots are converted from the one-minute sustained wind speed to the one-hour averaged wind speed by using the World Meteorological Organization's conversion factor of 1/1.11, as listed in Table 1.1 in Harper et al. (2010). The obtained snapshots based on the one-hour averaged wind speed for the two hurricane scenarios are presented in Figure 3.2 (the first column of figures).

To implement the developed TC model to simulate these two hurricane scenarios, first, the parameters (p_c, V_c, α) are extracted from the historical Best Track Data sets of the National Hurricane Center's Hurricane Databases (HURDATA) (Landsea and Franklin, 2013), which are listed on the left side of Figure 3.2. R_{max} is inferred from the horizontal wind profile, which is an azimuthally average of the H*Wind snapshots. Holland's parameter B is directly calculated by Equation (6). The obtained one-hour resultant velocity contours on the horizontal plane at the height of 10 m are listed in Figure 3.2 and are compared with H*Wind snapshots.

In the resultant velocity contours extracted from the developed TC model, dense contour lines are observed at the TC center, which means the resultant velocity quickly changes along the radial distance at the TC center. This is consistent with the phenomena observed in the results extracted from H*Wind snapshots for the two hurricanes. In Hurricane Katrina (2005), the maximum wind speed of the simulated TC is about 60 m/s, which is very close to that extracted from the H*Wind snapshot. To facilitate comparing the magnitudes of individual resultant velocities on the horizontal plane, the correlation of individual velocities on the horizontal plane are calculated and presented in Figure 3.2. The R value for Hurricane Katrina is 0.957, which indicates that the wind velocity on the horizontal plane falls between the simulation using the developed model and the H*Wind snapshots. For Hurricane Irene (2011), the difference of the maximum wind speed between the simulated result and H*Wind snapshot is only about 3 m/s. The R value for Hurricane Irene (2011) is 0.927, indicating the good match.

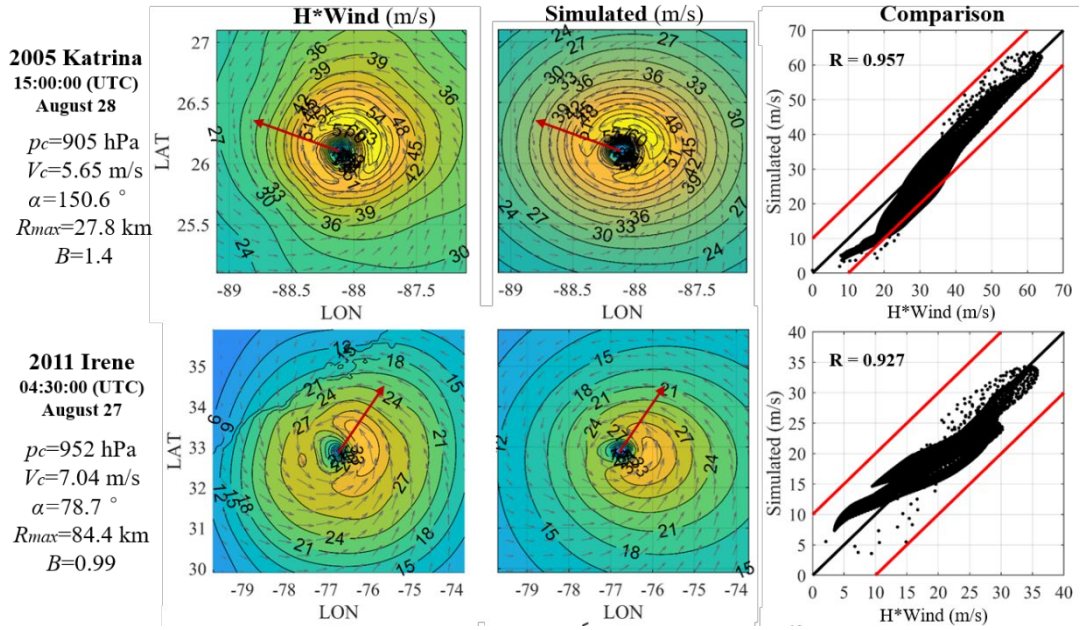

Figure 3.2 Comparisons of wind snapshots at 10 m for over ocean condition. Input parameters are listed on the left side. R on the right side is the Pearson correlation between the H*Wind and simulated wind. The red arrows are the TC moving directions.

For each hurricane scenario, the azimuthally averaged wind speed profiles along the radial distance are extracted from the simulated and H*Wind snapshots in Figure 3.2, respectively, and are compared in Figure 3.3. With the increase of the radial distance, the wind speed increases linearly and reaches its maximum value at the R_{max}, then it decreases gradually. Specifically, for Hurricane Katrina (2005) in Figure 3.3(a), the R_{max} of the simulated result is 30 km, which matches H*Wind. However, the wind speed obtained from the simulated TC is higher than that of H*Wind within the radial distance of 100 km, and it becomes smaller when the radial distance is greater than 100 km. For Hurricane Irene (2001), the R_{max} of the simulated results are about 65 km, which is smaller than the 84.4 km in H*Wind snapshots. In Figure 3.3(b), the simulated wind speed is slightly higher than that of H*Wind. These deviations are acceptable considering that only dynamic processes are included and empirical equations are used in the developed TC model.

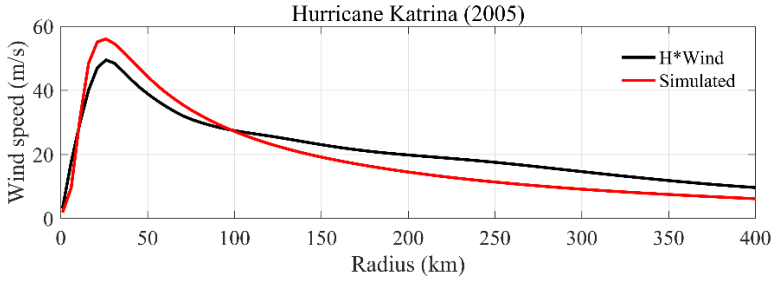

(a)

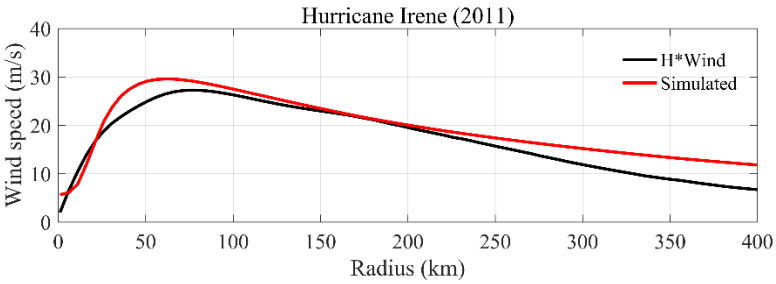

(b)

Figure 3.3 Comparisons of the azimuthally averaged wind speed along radial distance between the H*Wind and simulated hurricane snapshots shown in Figure 3.2.

3.3 Simulation of TC moving over the land

For landfall TCs, the influence of varying land cover and terrain on the behavior of hurricanes is significant. A series of simulations adding varying land cover and terrain to the developed TC model are carried out. Typhoon Mangkhut (2018) was one of the worst typhoon landfalls on the Pearl River Delta. Figure 3.4 shows the track of Typhoon Mangkhut (2018) and its atmospheric information. At the time of 09:00:00 (UTC) on September 16, 2018, this typhoon landed at Jiangmeng, Guangdong Province, with part of its wind field over the ocean and part over the land.

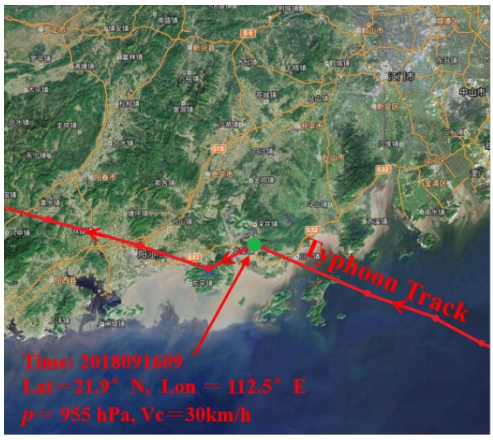

Figure 3.4 Track of Typhoon Mangkhut (2018) and related atmospheric information at 09:00:00 (UTC) on September 16, 2018.

The developed TC model is used to simulate Typhoon Mangkhut (2018) over the Pearl River Delta. The parameters of R_{max} and B are calculated by Equation (5) and Equation (6), respectively. The surface roughness length and the terrain height needed in Equation (14) and Equation (20) can be looked up from Figure 2.4(a) and Figure 2.4(b), respectively. The resultant velocity contours on the horizontal plane at four representative heights for the time instant of 09:00:00 (UTC) on September 16, 2018, are presented in Figure 3.5. Figure 3.5(a) is for the case with a constant roughness length (z_0=0.0002) and constant terrain height (z_s=0), which is the same as over the ocean, designated as No_LC_No_Ter. Figure 3.5(b) considers the varying land cover (z_0=Figure 2.4(a)), with a constant terrain height (z_s=0), designated as LC_No_Ter. Figure 3.5(c) considers the varying terrain height (z_s=Figure 2.4(b)), with a constant land cover (z_0=0.0002), designated as Ter_No_LC. Figure 3.5(d) is for the case with varying land cover and terrain, designated as LC_Ter.

Comparing with ocean conditions (Figure 3.5(a)), the inclusion of land cover and terrain (Figure 3.5(d)) can lead to a decrease of wind speed over land. Near the ground surface (at the height of 10 m and 100 m), Figure 3.5(d) shows that the maximum wind speed occurs over the

ocean. However, as the height increases (at the height of 500 m and 1000 m), the maximum wind speed occurs on land, which is nearly at the same position as in Figure 3.5(a). This indicates that the influence of varying land cover and terrain on TC wind speed decreases with the increase of height. By comparing Figure 3.5(a) with Figure 3.5(b), it shows that the varying land cover has little influence on TC wind fields above 500 m. However, for the terrain, its effect decreases much slower (Figure 3.5(c)), which is mainly because the terrain feature decays linearly with height in this terrain-following coordinate system and the high vertical extent height set in Equation (20) leads to a low decay rate.

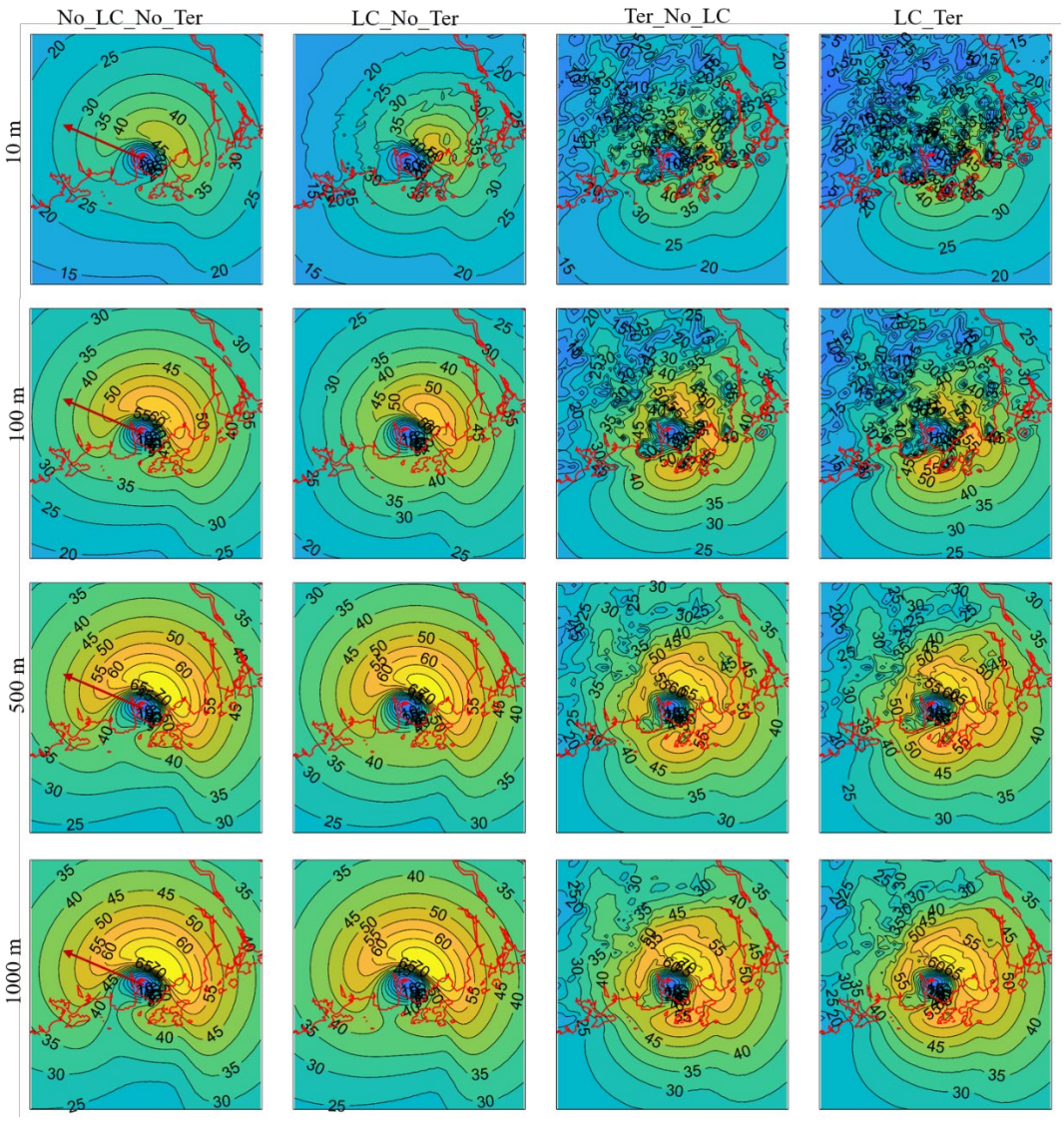

(a) (b) (c) (d)

Figure 3.5 Comparisons of resultant wind velocities on the horizontal planes of Typhoon Mangkhut (2018) over Pearl River Delta under different land cover and terrain situations at heights of 10 m, 100m, 500m, and 1000m at the time of 09:00:00 (UTC) on September 16, 2018. Coastlines are shown by the red lines and the red arrows are the TC moving directions. (a) Constant land cover and flat lower boundary, which are the same to the ocean condition (No_LC_No_Ter). (b) Varying land cover types with flat bottom boundary (LC_No_Ter). (c) Varying terrain with uniform land cover (Ter_No_LC). (d) Varying land cover and terrain (LC_Ter).

To further demonstrate the effects of varying land cover and terrain height, the wind speeds on the horizontal plane at the height of 10 m under the situation of (a) in Figure 3.5 are

taken as the reference, the wind speeds under the situations of (b), (c) and (d) are normalized, as presented in Figure 3.6. The ratio of LC_No_Ter to No_LC_No_Ter (Figure 3.6(a)) shows a reduction of wind speed induced by land cover, with a reduction factor of about 0.8 in coastal areas and a reduction factor of about 0.7 in inland areas. However, the wind speeds over the ocean in the south are slightly increased. Figure 3.6(b) presents the ratio of Ter_No_LC to No_LC_No_Ter. The varying terrain height shows the blocking effect on wind speed in Figure 3.6(b). In the high topographic area, the reduction factor is approximately 0.5, and it becomes 0.8 in the flat area. Wind speed accelerations are also observed in some isolated areas over the land, as indicated in Figure 3.6(b). With the terrain simulated, the increase of wind speeds over the ocean in the south is more significant than the effect of land cover. The coupled land cover and terrain show large wind reduction over the land (Figure 3.6(c)). The wind reduction factor in most land areas is lower than 0.5, while the increase of wind speeds over the ocean in the south is the most significant among the three cases.

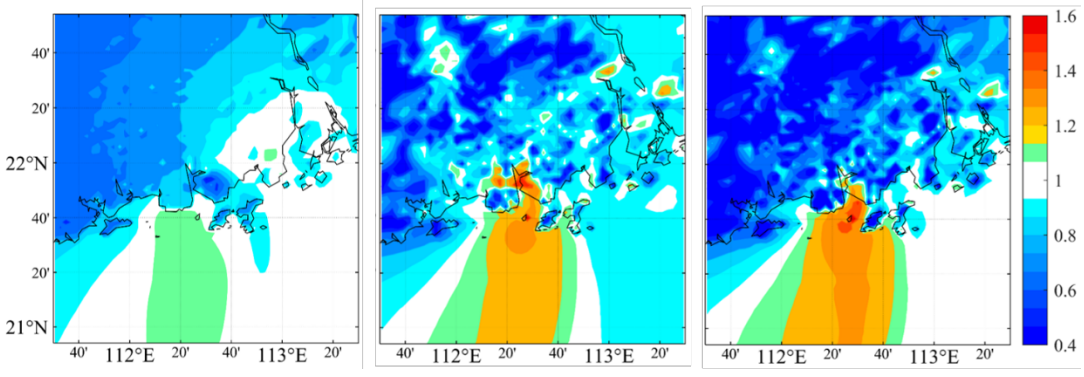

(a) (b) (c)

Figure 3.6 Normalized wind speeds under different situations of Typhoon Mangkhut (2018) in Figure 3.5. (a) Ratio of wind speed between LC_No_Ter and No_LC_No_Ter at the height of 10 m. (b) Ratio of wind speed between Ter_No_LC and No_LC_No_Ter at the height of 10m. (c) Ratio of wind speed between LC_Ter and No_LC_No_Ter at the height of 10 m.

3.4 Time series of wind speeds and directions during TC landfall

The developed TC model not only can provide the horizontal and vertical wind speed fields, but can also produce the time history of wind speeds and directions during landfall. To validate the obtained time histories of wind speeds and directions, they are compared with the wind records of Hurricane Katrina (2005) obtained from the National Data Buoy Center (NDBC) (Meindl and Hamilton, 1992), and the observation data of Typhoons Hagupit (2008) and Hato (2017) obtained from the Guangdong Meteorological Service and Hong Kong Observatory, respectively.

The input data to the developed TC model are obtained from the historical Best Track Data sets. For Hurricane Katrina in 2005, the data is from the National Hurricane Center's Hurricane Databases (HURDAT) (Landsea and Franklin, 2013); for Typhoons Hagupit (2008) and Hato (2017), the data are from the CMA Tropical Cyclone Data Center (Ming et al., 2014). The center locations and pressures of TCs in these Best Track Data sets are interpolated linearly to a one-hour scale. The datasets of land cover and terrain height used here are the same as those presented in Section 2.5. With the obtained input data, the time histories of wind speeds and directions at Stations of 42040 for Hurricane Katrina (2005), Shangchuandao for Typhoon Hagupit (2008), and Henglandao for Typhoon Hato (2017) during TC landfall are extracted from the developed TC model, and compared with the observation data, as shown in Figure 3.6. These three stations are indicated as green diamonds in Figure 3.6.

In Figure 3.6, the simulated results are plotted as a red solid graph. As the TC moves from the ocean to the land, the distance from the observation station to the TC center becomes shorter, and the wind speed gradually increases, and reaches the maximum wind speed at about 12:00:00 (UTC) on August 29 for Hurricane Katrina (2005), 19:00:00 (UTC) on September 23

for typhoon Hagupit (2008), and 02:00:00 (UTC) on August 23 for typhoon Hato (2017). Then, the wind speed gradually decreases as the TC moves away. The simulation results in Figure 3.6 show that simulated wind speeds and directions match reasonably well with the observed data, considering the neglect of thermodynamics and the uncertainties of local environments. This indicates that the numerical TC model developed in this study is capable of simulating TC wind fields in space and time.

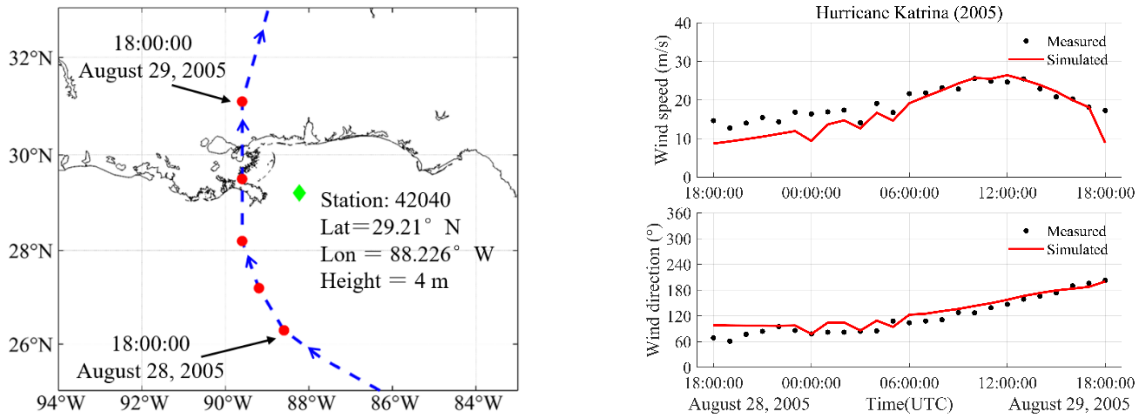

(a)

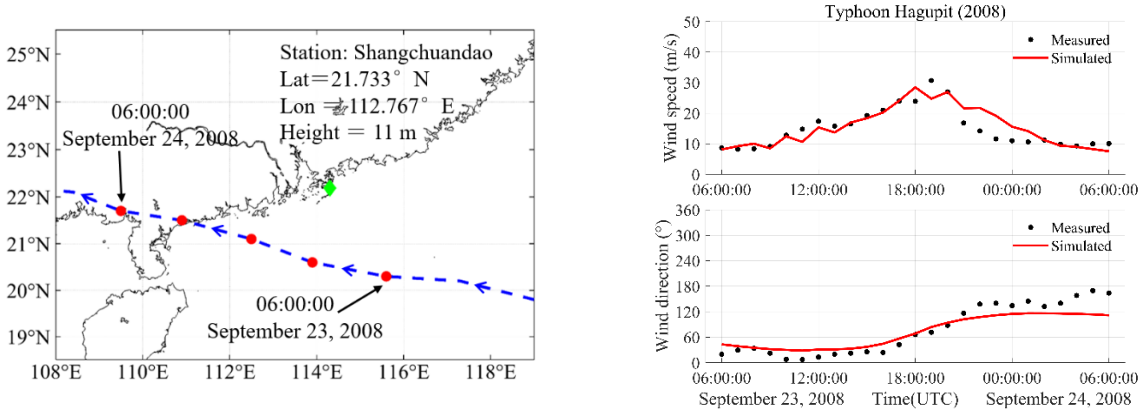

(b)

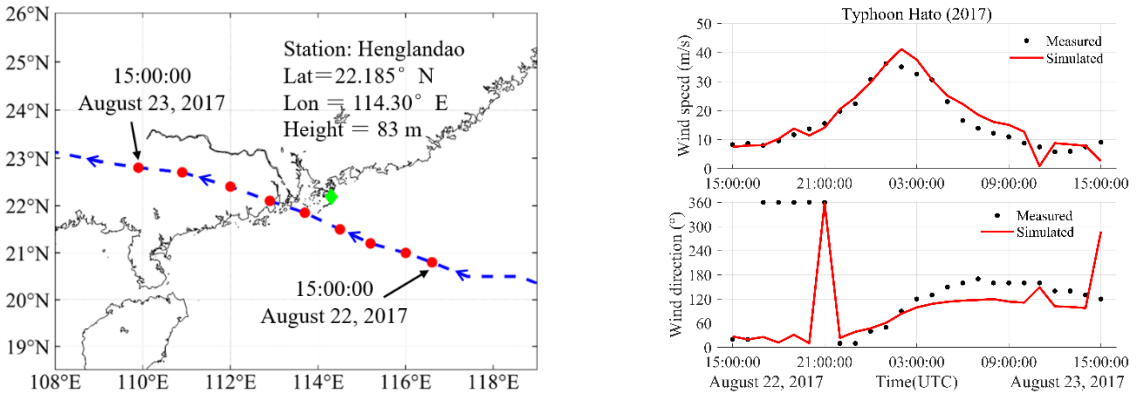

(c)

Figure 3.7 Comparisons of the simulated wind speeds (right top) and directions (right bottom) with the observation data of (a) Hurricane Katrina (2005), (b) Typhoon Hagupit (2008), (c) Typhoon Hato (2017). Left column is the corresponding TC tracks and observation stations' information; blue dash lines mean the track of the TC; red dots denote the location of TC center; green diamonds represent the location of the weather sounding station; dates represent the start and end times for comparisons, respectively.

Chapter 4 Conclusions

In this project, a high-fidelity, high-efficiency numerical TC model has been developed to simulate TCs and investigate wind characteristics of TCs. This model is based the Boussinesq Approximation and Reynolds Averaging and is built on a terrain-following coordinate system, which facilitates studying the effects of varying land cover and terrain on TC wind characteristics. To improve computational efficiency, a sophisticated boundary layer turbulence closure scheme is adopted, and a nested horizontal grid system is applied. The following conclusions can be drawn.

(1) Sensitivity studies demonstrate that the simulation duration of 10 hours is long enough to form a TC vortex and reach a steady state. By comparing four different grid systems, the nested grid system with $dx=dy=0.1R_{max}$ as the grid distance and $2R_{max}\times 2R_{max}$ as the area of the innermost nest is suitable to produce reliable results.

(2) The wind velocity profile along height extracted from the developed TC model follows the log law for lower elevations. In addition, the boundary layer turbulence closure scheme, especially the vertical eddy viscosity coefficient K_V, significantly affects the wind velocity profile along height; and a constant K_V value that was often used in previous studies leads to an incorrect wind velocity profile.

(3) The wind velocity distribution on horizontal plans obtained from the developed TC model matches reasonably well the H*Wind snapshots.

(4) After a TC landfall, the inclusion of land cover and terrain leads to a decrease of wind speed over land. Although both the varying land cover and terrain affect TC wind fields, the influence of terrain is more significant than land cover. The influence of the varying land cover and terrain gradually decreases with the increase of height.

(5) The developed TC model successfully reproduces the time histories of wind speeds and directions for Hurricane Katrina (2005), Typhoon Hagupit (2008), and Typhoon Hato (2017). This demonstrates the capability of the developed TC model to provide simulation results of wind fields in space and time.

The TC model developed in this study offers a useful tool to reproduce TC wind fields under different land cover and terrain conditions. In future studies, thermal equations will be incorporated into the TC model and the TC-related disaster modeling, such as TC-related rainfall and storm surge, will be investigated.

References

Batts, M.E., ASCE, A.M., Russell, L.R., Simiu, E., 1980. Hurricane Wind Speeds in The United States. Journal of Structural Division 106, 2001-2016.

Blackadar, A., 1976. Modeling the Nocturnal Boundary Layer. Proc. of Third Symposium on Atmospheric Turbulence, Diffusion and Air Quality, 46-49.

Chow, S.H., 1971. A study of the wind field in the planetary boundary layer of a moving tropical cyclone, Graduate Division of the School of Engineering and Science. New York University, New York.

Done, J.M., Ge, M., Holland, G.J., Dima-West, I., Phibbs, S., Saville, G.R., Wang, Y., 2020. Modelling global tropical cyclone wind footprints. Natural Hazards and Earth System Sciences 20, 567-580.

ESA, 2017. Land Cover CCI: Product User Guide Version 2.0. Tech. Rep. Available at: maps.elie.ucl.ac.be/CCI/viewer/download/ESACCI-LC-Ph2-PUGv2_2.0.pdf.

Fang, G., Zhao, L., Cao, S., Ge, Y., Pang, W., 2018a. A novel analytical model for wind field simulation under typhoon boundary layer considering multi-field correlation and height-dependency. Journal of Wind Engineering and Industrial Aerodynamics 175, 77-89.

Fang, G., Zhao, L., Song, L., Liang, X., Zhu, L., Cao, S., Ge, Y., 2018b. Reconstruction of radial parametric pressure field near ground surface of landing typhoons in Northwest Pacific Ocean. Journal of Wind Engineering and Industrial Aerodynamics 183, 223-234.

Franklin, J.L., Black, M.L., Valde, K., 2003. GPS Dropwindsonde Wind Profiles in Hurricanes and Their Operational Implications. Weather and Forecasting 18, 32-44.

Gal-Chen, T., Somerville, R.C.J., 1975. On the use of a coordinate transformation for the solution of the Navier-Stokes equations. Journal of Computational Physics 17, 209-228.

Galperin, B., Kantha, L.H., Hassid, S., Rosati, A., 1988. A Quasi-equilibrium Turbulent Energy Model for Geophysical Flows. 45, 55-62.

Georgiou, P.N., Davenport, A.G., Vickery, B.J., 1983. Design wind speeds in regions dominated by tropical cyclones. Journal of Wind Engineering and Industrial Aerodynamics 13, 139-152.

Giammanco, I.M., Schroeder, J.L., Powell, M.D., 2013. GPS Dropwindsonde and WSR-88D Observations of Tropical Cyclone Vertical Wind Profiles and Their Characteristics. Weather and Forecasting 28, 77-99.

Grell, G.A., Dudhia, J., Stauffer, D.R., 1994. A Description of the Fifth-Generation Penn State/NCAR Mesoscale Model (MM5). NCAR Technical Note.

Harper, B., Kepert, J., Ginger, J., 2010. 2009: Guidelines for Converting Between Various Wind

Averaging Periods in Tropical Cyclone Conditions.

Holland, G.J., 1980. An analytic model of the wind and pressure profiles in hurricanes. Monthly Weather Review 108, 1212-1218.

Holton, J.R., 2007. An Introduction to Dynamic Meteorology (Fourth Edition). Elsevier Academic Press, Boston.

Hong, X., Hong, H.P., Li, J., 2019. Solution and validation of a three dimensional tropical cyclone boundary layer wind field model. Journal of Wind Engineering and Industrial Aerodynamics 193, 103973.

Kepert, J., 2001. The Dynamics of Boundary Layer Jets within the Tropical Cyclone Core. Part I: Linear Theory. Journal of the Atmospheric Sciences 58, 2469-2484.

Kepert, J., Wang, Y., 2001. The Dynamics of Boundary Layer Jets within the Tropical Cyclone Core. Part II: Nonlinear Enhancement. Journal of Atmospheric Sciences 58, 2485-2501.

Kepert, J.D., 2012. Choosing a Boundary Layer Parameterization for Tropical Cyclone Modeling. Monthly Weather Review 140, 1427-1445.

Landsea, C.W., Franklin, J.L., 2013. Atlantic Hurricane Database Uncertainty and Presentation of a New Database Format. Monthly Weather Review 141, 3576-3592.

Li, S.H., Hong, H.P., 2015. Observations on a Hurricane Wind Hazard Model Used to Map Extreme Hurricane Wind Speed. Journal of Structural Engineering 141, 1-12.

Meindl, E.A., Hamilton, G.D., 1992. Programs of the National Data Buoy Center. Bulletin of the American Meteorological Society 73, 985-994.

Mellor, G.L., Yamada, T., 1974. A Hierarchy of Turbulence Closure Models for Planetary Boundary Layers. Journal of the Atmospheric Sciences 31, 1791-1806.

Meng, Y., Masahiro, M., Kazuki, H., 1995. An analytical model for simulation of the wind field in a typhoon boundary layer. Journal of Wind Engineering and Industrial Aerodynamics 56, 291-310.

Meng, Y., Masahiro, M., Kazuki, H., 1997. A numerical study of the wind field in a typhoon boundary layer. Journal of Wind Engineering and Industrial Aerodynamics 67-68, 437-448.

Ming, Y., Wei, Z., Hui, Y., Xiaoqin, L., Feng, J., Fan, Y., Zhu, Y., Chen, D., 2014. An Overview of the China Meteorological Administration Tropical Cyclone Database. Journal of Atmospheric and Oceanic Technology 31, 287-301.

Orlanski, I., 1976. A simple boundary condition for unbounded hyperbolic flows. Journal of Computational Physics 21, 251-269.

Powell, M.D., Houston, S.H., Amat, L.R., Morisseauleroy, N., 1998. The HRD real-time

hurricane wind analysis system. Journal of Wind Engineering and Industrial Aerodynamics 77&78, 53–64.

Powell, M.D., Vickery, P.J., Reinhold, T.A., 2003. Reduced drag coefficient for high wind speeds in tropical cyclones. Nature 422, 279-283.

Skamarock, W.C., Klemp, J.B., Dudhia, J., Gill, D.O., Liu, Z., Berner, J., Wang, W., Powers, J.G., Duda, M.G., Huang, X.Y., 2019. A Description of the Advanced Research WRF Model Version 4. No. NCAR/TN-556+STR.

Smagorinsky, J., Manabe, S., Holloway, J.L., 1965. Numerical Results from a Nine-Level General Circulation Model of the Atmosphere. Monthly Weather Review 93, 727-768.

Snaiki, R., Wu, T., 2017a. A linear height-resolving wind field model for tropical cyclone boundary layer. Journal of Wind Engineering and Industrial Aerodynamics 171, 248-260.

Snaiki, R., Wu, T., 2017b. Modeling tropical cyclone boundary layer: Height-resolving pressure and wind fields. Journal of Wind Engineering and Industrial Aerodynamics 170, 18-27.

Tan, C., Fang, W., 2018. Mapping the Wind Hazard of Global Tropical Cyclones with Parametric Wind Field Models by Considering the Effects of Local Factors. International Journal of Disaster Risk Science 9, 86-99.

Thompson, E.F., Cardone, V.J., 1996. Pratical modeling of hurricane surface wind fields. Journal of Waterway Port Coastal & Ocean Engineering 122, 195-205.

Vickery, P.J., Lin, J., Skerlj, P.F., Twisdale, L.A., Huang, K., 2006. HAZUS-MU Hurricane Model Methodology. I: Hurricane Hazard, Terrain, and Wind Load Modeling. Natural Hazards Review 7, 82-93.

Vickery, P.J., Skerlj, P.F., Steckley, A.C., Twisdale, L.A., 2000. Hurricane Wind Field Model for Use in Hurricane Simulations. Journal of Structural Engineering 126, 1203-1221.

Vickery, P.J., Wadhera, D., 2008. Statistical Models of Holland Pressure Profile Parameter and Radius to Maximum Winds of Hurricanes from Flight-Level Pressure and H*Wind Data. Journal of Applied Meteorology and Climatology 47, 2497-2517.

Vickery, P.J., Wadhera, D., Powell, M.D., Chen, Y., 2009. A Hurricane Boundary Layer and Wind Field Model for Use in Engineering Applications. Journal of Applied Meteorology and Climatology 48, 381-405.

Wu, F., Huang, G., 2019. Refined Empirical Model of Typhoon Wind Field and Its Application in China. Journal of Structural Engineering 145, 04019122.

Yang, Y., Xiao, P., Feng, X., Li, H., 2017. Accuracy assessment of seven global land cover datasets over China. ISPRS Journal of Photogrammetry and Remote Sensing 125, 156-173.